Fermilab FERMILAB-FN-0745 April 2004

Non-Neutrino Particle Flux in the MINERνA Detector

M.A. Kostin and N.V. Mokhov
Fermilab, P.O. Box 500, Batavia, Illinois 60510

April 23, 2004

Abstract

Non-neutrino particle fluxes will be created in the NuMI near hall due to interactions of the neutrino beam in the surrounding rock. Results of MARS14-based studies of backgrounds in the MINERνA detector are presented in this report.

1 Introduction

The NuMI facility at Fermilab [1] will provide high intensity neutrino beams. This will give a great opportunity for non-oscillation neutrino physics. Whereas some of the non-oscillation physics topics can be addressed with the MINOS near detector, there is a need for a new one specifically designed for these purposes. The new detector should be made with a finer granularity and better resolution capabilities. The recently formed collaboration MINERνA (Main Injector ExpeRiment ν-A) [2] currently designs such a detector, that can be used for a broad range of non-oscillation topics. Some of those are sensitive to background particles created in neutrino interactions, particularly, to neutrons. The background will be created in interactions of the neutrino beam in the rock surrounding the NuMI near hall. In this report, results of background studies are presented.

2 Geometry Model

Background particle fluxes were studied with the MARS14 code [3]. The MARS14-based model includes both the MINOS and MINERνA detectors in the NuMI near hall with the surrounding dolomite rock (Figs. 1 and 2). The hall itself is approximately 46 m long, 9.6 m wide and 9.7 m high. There is an extra empty space right in the front of the hall that represents a simplified model of the beginning of bypass. It is 26 m long and 8.5 m wide. The hight varies from 8.1 m in the most upstream part to 6.7 m in the front of the hall. There is 50 m of the dolomite rock in the model further upstream. The choice of the given rock thickness in the model is based on the fact that there will not be any particles produced more than 50 m upstream, beside the neutrinos, that are able to reach the hall. In order to justify the above, let us estimate the maximum energy of muons at which those can penetrate through 50 m of rock. In the case when only the ionization losses contribute to the muon degradation, the maximum energy is $dE/dx * \rho(rock) * length \approx 2$ MeV/(g/cm^2) * 2.85 g/cm^3 * 50 m = 28.5 GeV. A fraction of neutrinos, and hence muons, with the energy higher than that is negligible at NuMI running conditions [4]. Direct MARS14 simulations confirm that no muons from the NuMI beam line reach the hall. All other types of particles have even higher degradation rates.

Both the detectors are placed on the NuMI axis descending at an angle of 3 degrees with respect to the near hall axis, so that the most intense part of the neutrino beam comes through the detectors. The MINOS near detector can be simplified in the model because only low-energy albedo particles can contribute to backgrounds in the MINERνA detector. It is a solid chunk of steel of approximately correct geometry (Fig. 3) [5]. There are no scintillator pads and gaps between steel plates in the model. The steel density is reduced to $\rho = 3.37\ g/cm^3$ in order to compensate for the plastic and air gaps. In the real detector, the 2.5-cm thick steel plates are interchanged with the 1 cm scintillator pads. As one can see, there is more steel than scintillator in the detector. Moreover, the mean free path in steel is about 5 times shorter than in the scintillator. For instance, the inelastic mean free path for a 5-GeV neutron in steel is $\approx$ 15 cm, whereas it is $\approx$ 78 cm in the scintillator. Therefore, the scintillator can be omitted from the model for the sake of simplicity.

The MINERνA detector is described in details in the proposal [6]. It has a hexagonal

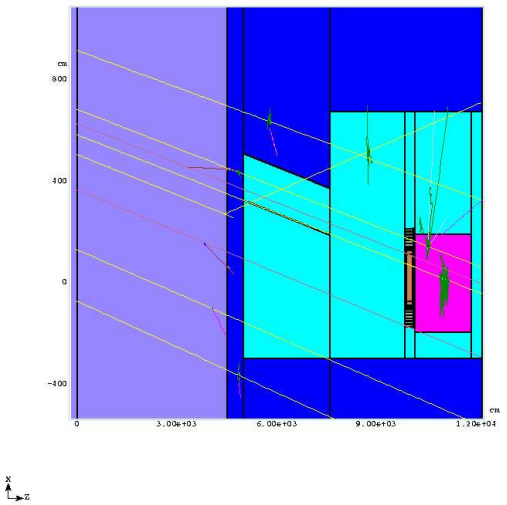

Figure 1: Elevation view of the NuMI near hall. Tracks of neutrinos and products of their interactions are shown.

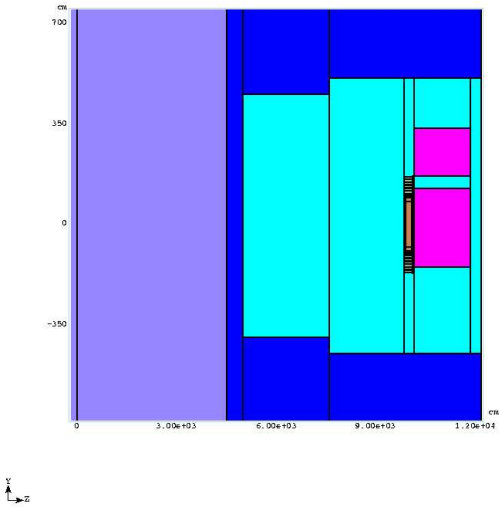

Figure 2: Horizontal view of the NuMI near hall.

cross-section (Fig. 5). The most internal part of the detector (active target) is scintillator with the "radius" of a diagonal of 92.5 cm and the length of 2 m. The following 15 cm along the diagonal is an EM calorimeter. The calorimeter is made of many longitudinal layers, where each of them is a 1.5 cm thick scintillator plane followed by 2 mm of lead. The next part is a barrel of hadronic calorimeter sandwich. The sandwich consists of ten scintillator-steel layers. The first four layers have 1.5 cm of scintillator and 2.5 cm of steel each. The thickness of steel is increased to 10 cm for the following six layers. The detector starts and ends with two hadronic calorimeters with vertical scintillator bars (Fig. 4). The first calorimeter is placed inside the barrel. Each of them has the total thickness of steel of 50 cm. The calorimeters are separated from the active target with 2 cm thick lead plates. The lead plates represent electromagnetic calorimeters. The scintillator bars in the front and end hadronic calorimeters are omitted from the model. Those in the barrel are left for trigger studies. No magnetic field in both the detectors was used for simulations.

3 Neutrino Beams in the Model

Neutrinos arrive at the near hall from the NuMI channel [1]. The NuMI beamline delivers 120 GeV/c proton beam from the Fermilab Main Injector onto a graphite target of approximately two interaction lengths long. The secondaries produced in the target are focused then by two magnetic horns and enter the decay volume 50 m downstream of the target. The neutrinos are produced there mostly from pions and kaons decays. The decay volume is a cylindrical vacuum vessel of 2 m in diameter and 675 m long. A 10 m long hadron absorber stops undecayed secondaries and uninteracted primary protons at the end of the decay pipe. The following 240 m of dolomite rock range out the muons before the neutrino beam enters the NuMI near hall.

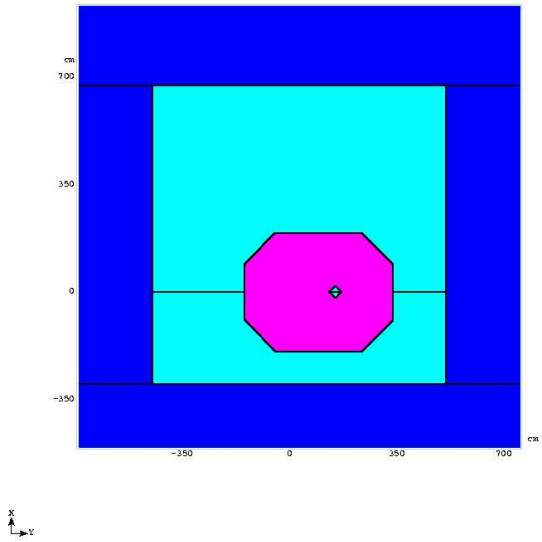

Figure 3: Cross-section of the MINOS near detector and the hall (looking downstream).

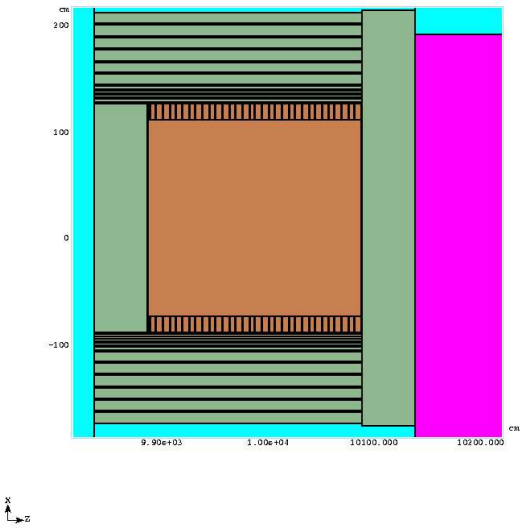

Figure 4: Elevation view of the MINERνA detector.

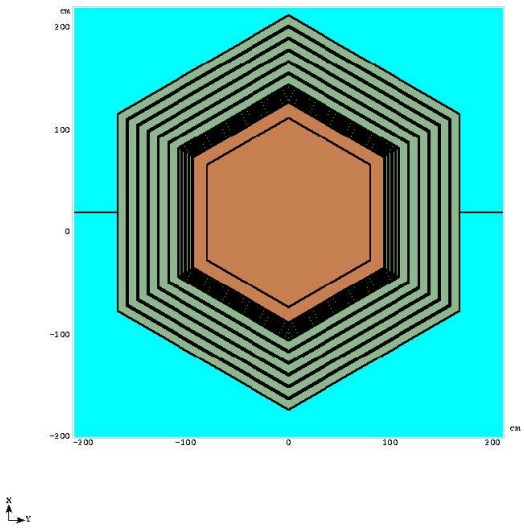

Figure 5: Cross-section of the MINERνA detector.

The energy of the neutrino beam is controlled by the positions of target and second horn. Originally three energy options were considered: Low Energy (LE), Medium Energy (ME) and High Energy (HE). It has been found, however, that moving the second horn would result in a significant downtime and a loss of beam time. As an alternative, it has been proposed to move the target only to change the peak energy of the beam [4], even though it would result in a lower neutrino flux. This can be accomplished remotely with a maximal target shift of -2.5 m with respect to the original position. The configurations

corresponding to the shifts of -1.0 m and -2.5 m are called “semi-medium” and “semi-high” energy beam tunes. LE, semi-ME and semi-HE beam tunes were used for these studies. Various neutrino distributions at the near hall are shown in Figs. 6-8. The plots are normalized to the number of protons on target in one spill. The proton intensity is assumed to be 2×10^{13} protons/spill. As one can see, the beam becomes narrower as its energy increases (Fig. 8). There is a minor admixture of other types of neutrinos from various pion, kaon and muon decays (Fig. 9).

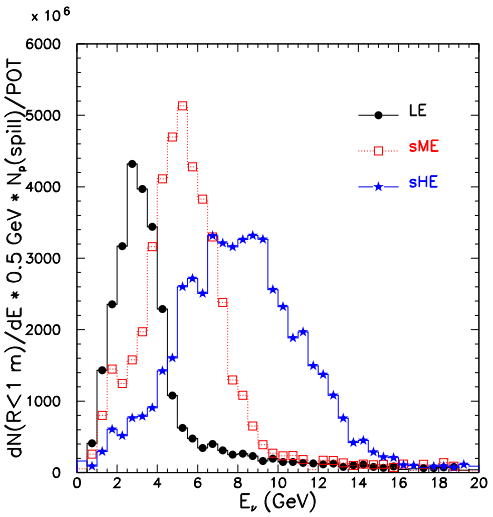

Figure 6: Muon neutrino energy distributions at the near detector hall within a distance of 1 m about the axis of NuMI.

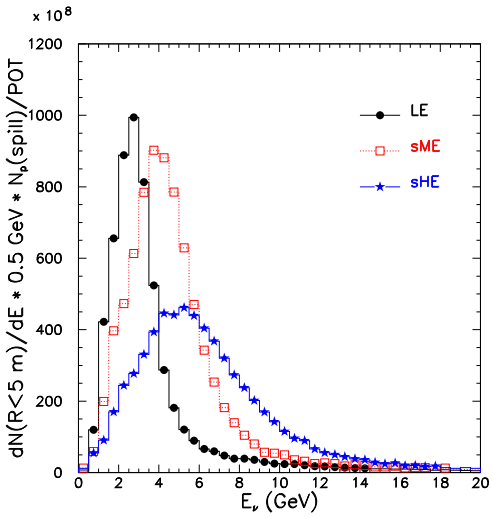

Figure 7: Muon neutrino energy distributions at the near detector hall within a distance of 5 m about the axis of NuMI.

4 Neutrino Interaction Model in MARS14

A comprehensive description of the MARS neutrino interaction model can be found in Ref. [7]. Briefly, the model tracks the energy and angle of final state neutrinos, hadrons, $e^{\pm}$, and $\mu^{\pm}$ from neutrino interactions. These particles, together with the showers they initiate, are transported through the user-defined geometry, and energy deposition and dose are calculated. MARS distinguishes four types of neutrinos: ν_μ, $\overline{\nu}_\mu$, ν_e and $\overline{\nu}_e$. All four types are found in the neutrino beam. The model identifies *eight* types of interactions for ν_μ and $\overline{\nu}_\mu$. Those are summarized in Table 4. There is an entirely similar list for ν_e and $\overline{\nu}_e$. Only the recoil is simulated for all the ’elastic’ interactions. The model does not include inelastic neutrino interactions which produce pions via resonances. The process of hadronization is simplified for charged-current DIS (process 1): once the momentum of lepton is decided on, the total momentum is balanced by a single pion, which is forced to undergo a deep-inelastic interaction in the same nucleus. This coarse “hadronization” is justifiable since we are interested in certain gross averages over the showers.

All the neutrinos are forced to interact in the simulated system. A vertex is randomly chosen along a straight line that would represent a neutrino track in case when the given

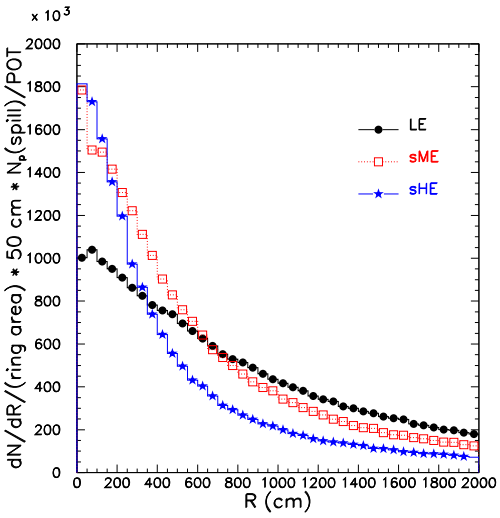

Figure 8: Muon neutrino radial distributions at the near detector hall. The origin corresponds to the NuMI axis.

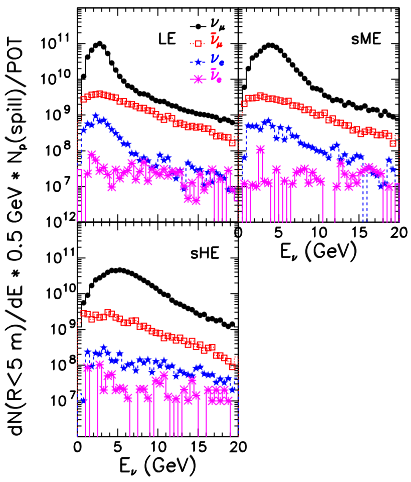

Figure 9: Neutrino beam composition.

Table 1: ν_μ and $\overline{\nu}_\mu$ interaction processes in the MARS14 code.

#	process	ν interaction	$\overline{\nu}$ interaction
1)	CC DIS	$\nu_\mu N \to \mu^- X$	$\overline{\nu}_\mu N \to \mu^+ X$
2)	NC DIS	$\nu_\mu N \to \nu_\mu X$	$\overline{\nu}_\mu N \to \overline{\nu}_\mu X$
3)	νN el, qel	$\nu_\mu n \to \mu^- p$	$\overline{\nu}_\mu p \to \mu^+ n$
4)	νN el, qel	$\nu_\mu p \to \nu_\mu p$	$\overline{\nu}_\mu p \to \overline{\nu}_\mu p$
5)	νN el, qel	$\nu_\mu n \to \nu_\mu n$	$\overline{\nu}_\mu n \to \overline{\nu}_\mu n$
6)	ν atomic e	$\nu_\mu e^- \to \nu_\mu e^-$	$\overline{\nu}_\mu e^- \to \overline{\nu}_\mu e^-$
7)	ν atomic e	$\nu_\mu e^- \to \nu_e \mu^-$	
8)	Coherent elastic	$\nu_\mu A \to \nu_\mu A$	$\overline{\nu}_\mu A \to \overline{\nu}_\mu A$

neutrino did not interact in the system. An appropriate weight is assigned to each neutrino interaction: $w = (l_i/\lambda_i)/\sum_{i=1}^{N}(l_i/\lambda_i)$, where i is the index of material in which the interaction occurs, N is the total number of materials encountered by the straight line, l_i is the length of block along the line in the i-th material, and λ_i is a corresponding interaction length.

5 Simulation Results

A set of simulation runs has been performed for the LE, sME and sHE beam configurations. Particle fluxes averaged over the volume of active target for various threshold kinetic energies are summarized in Tables 2-4. The tables contain three columns for the fluxes titled 'XX tot', 'XX sig' and 'XX sig 2'. Those refer to the fluxes in the active target due to

particles generated respectively anywhere in the system (total fluxes), forward calorimeter and the active target, and the active target only.

Energy dependences of the total fluxes are shown in Figs. 10-14. The dependences are represented for various beam configurations and classes of particles such as neutrons, charged hadrons, muons, photons and electrons/positrons. The plots illustrate the traits seen in the tables. For example, the photon spectrum drops quickly with the energy, so that even a small energy cut provides a significant photon background reduction. Muons, on the other hand, are generated mostly in the reactions of CC DIS and ν N quasi-elastic scattering, that produce muons of higher momenta.

The shapes of the spectra for neutrons, charged hadrons, γ, and $e^{\pm}$ are similar for all the beam configurations. Qualitatively, the neutrons and hadrons are originated in the 'lower' vertex and their energy spectra are quite insensitive to the beam energy. The weak energy dependence is further washed out by the consequent hadronic cascades. The γ and $e^{\pm}$ are generated from the hadronic showers via π^0 decays. Therefore the above is equally true for them.

Figs. 15-34 demonstrate flux distributions for various classes of particles. The distributions are obtained for the LE beam. Distributions for the sME and sHE beams are similar. There are four plots for each particle class. The first plot represents a flux distribution over a NuMI hall cross-section. The fluxes in the histogram bins are averaged over the thickness of the active target. The second plot is a flux distribution azimuthally averaged about the axis of the detector. The first two plots in the set are for the threshold kinetic energy of E_{th}=0.1 MeV. The second two plots are similar to the first ones but for the threshold kinetic energy of E_{th}=20 MeV.

6 Conclusions

A major conclusion of this report is that background particle fluxes are relatively low in the MINERνA detector. For example, for the LE beam configuration, an averaged track length for neutrons in the active target for $E_{th} = 20\ MeV$ is $F_n \times V_{target} = 1.26 \times 10^{-5}\ cm^{-2} \times 6.2 \times 10^6\ cm^3 = 78.1\ cm$. The inelastic mean free path for neutrons of the most probable energy of 80 MeV (see Fig. 10) is 83.8 cm in the plastic. This means that for the given detector geometry there are very few neutrons found in the active target each spill. Therefore, the probability to bind such a neutron to an event vertex by mistake should be rather small.

For the proposed MINERνA run, expected numbers of events per one ton are 100 k for quasi-elastic events, 420 k for DIS, 8 k for coherent pion production, and 406 k for resonances and transition region to DIS [6]. The fact that the resonances are not included into the model does not change the conclusion above, even though the particle flux underestimation may be as high as 40 % for the low energy region.

A complete simulation with the detector response and track reconstruction is desirable to see effects of the background on the physics analysis.

7 Acknowledgments

We are thankful to J.G. Morfin for initiating these studies, and for useful discussions and constructive comments.

References

[1] J. Hylen et al., “Conceptual Design for the Technical Components of the Neutrino Beam for the Main Injector (NuMI)”, FERMILAB-TM-2018, Sep. 1997.

[2] J. Arrington et al., Expression of Interest to Perform a High-Statistics Neutrino Scattering Experiment using a Fine-grained Detector in the NuMI Beam, Nov. 21, 2002.

[3] N.V. Mokhov, ”Status of MARS Code”, Fermilab-Conf-03/053, Apr. 2003; http://www-ap.fnal.gov/MARS/.

[4] M. Kostin et al., “Proposal for Continuously-Variable Beam Energy”, NuMI-B-783, Oct. 2001.

[5] MINOS Collaboration, MINOS Technical Design Report, NUMI-337, Oct. 1998.

[6] MINERνA Collaboration, Proposal, to be published.

[7] N.V. Mokhov and A. Van Ginneken, “Neutrino Radiation at Muon Colliders and Storage Rings”, FERMILAB-Conf-00/065, Apr. 2000.

Table 2: Particle fluxes averaged over the active target for the LE beams. E_{th} is a threshold kinetic energy used in the simulations.

Particle	E_{th} (MeV)	Flux ($10^{-5} cm^{-2}$)		
		LE tot	LE sig	LE sig 2
n	0.1	3.10	1.66	0.0465
	20	1.26	0.64	0.0271
	100	0.49	0.30	0.0140
Charged hadrons	0.1	0.66	0.67	0.0523
	20	0.73	0.63	0.0522
	100	0.55	0.59	0.0505
γ	0.1	15.94	10.30	0.3150
	20	1.08	0.99	0.0583
	100	0.26	0.21	0.0238
$e^{\pm}$	0.1	1.28	1.04	0.0614
	20	0.44	0.45	0.0436
	100	0.16	0.17	0.0163
$\mu^{\pm}$	0.1	1.43	0.62	0.0206
	20	1.41	0.61	0.0206
	100	1.40	0.62	0.0190

Table 3: Particle fluxes averaged over the active target for the sME beams. E_{th} is a threshold kinetic energy used in the simulations.

Particle	E_{th} (MeV)	flux ($10^{-5} cm^{-2}$)		
		sME tot	sME sig	sME sig 2
n	0.1	6.50	3.08	0.0986
	20	2.45	1.37	0.0586
	100	0.95	0.60	0.0258
Charged hadrons	0.1	1.39	1.21	0.1059
	20	1.34	1.11	0.1012
	100	1.10	0.99	0.0877
γ	0.1	33.64	27.29	0.6033
	20	1.63	1.84	0.1254
	100	0.41	0.48	0.0493
$e^{\pm}$	0.1	2.11	2.20	0.1272
	20	0.83	0.76	0.0717
	100	0.26	0.25	0.0318
$\mu^{\pm}$	0.1	2.61	1.25	0.0416
	20	2.58	1.31	0.0417
	100	2.59	1.28	0.0397

Table 4: Particle fluxes averaged over the active target for the sHE beams. E_{th} is a threshold kinetic energy used in the simulations.

Particle	E_{th} (MeV)	flux ($10^{-5} cm^{-2}$)		
		sHE tot	sHE sig	sHE sig 2
n	0.1	8.77	4.27	0.1351
	20	3.48	1.84	0.0822
	100	1.35	0.85	0.0355
Charged hadrons	0.1	2.04	1.77	0.1534
	20	1.93	1.65	0.1550
	100	1.57	1.47	0.1220
γ	0.1	46.26	34.65	0.9879
	20	2.20	2.18	0.1608
	100	0.51	0.55	0.0710
$e^{\pm}$	0.1	2.93	2.83	0.1554
	20	1.16	1.07	0.1038
	100	0.32	0.39	0.0480
$\mu^{\pm}$	0.1	3.08	1.58	0.0493
	20	3.09	1.63	0.0491
	100	3.07	1.59	0.0472

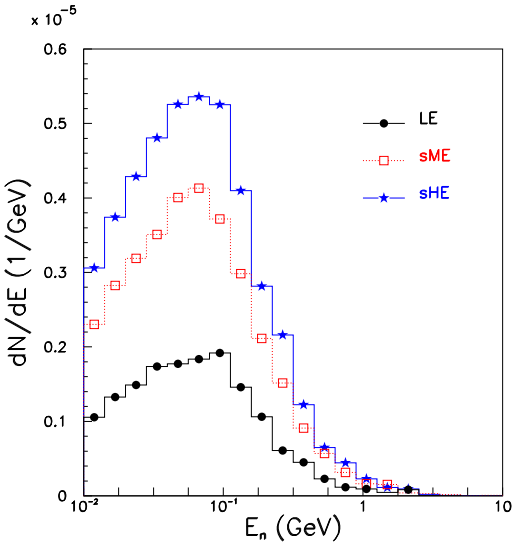

Figure 10: Energy dependence of the total flux of the neutrons for the LE, sME ans sHE beams.

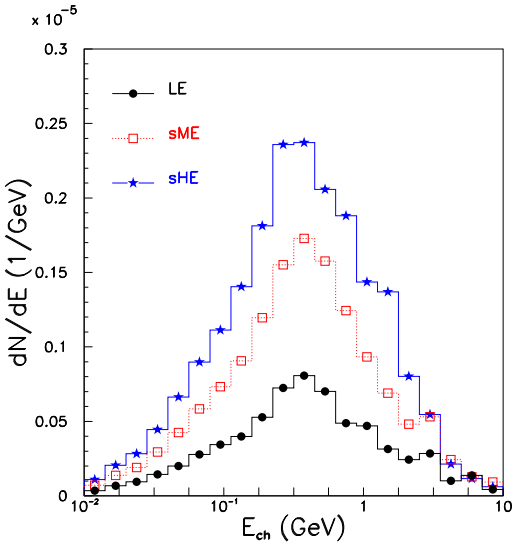

Figure 11: Energy dependence of the total flux of the charged hadrons for the LE, sME ans sHE beams.

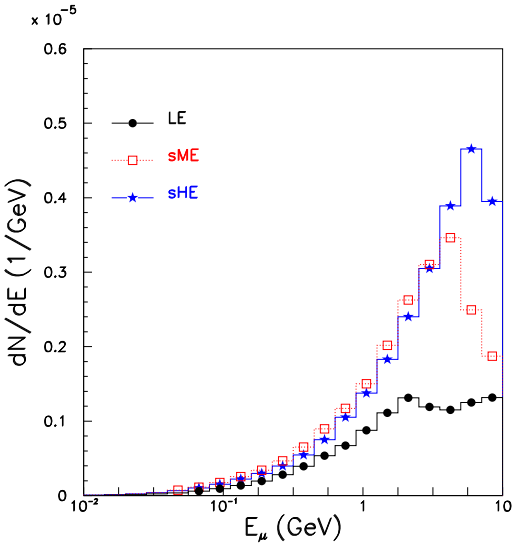

Figure 12: Energy dependence of the total flux of the muons for the LE, sME ans sHE beams.

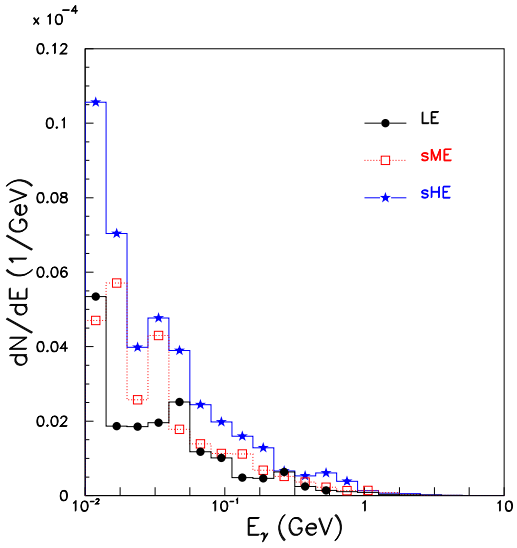

Figure 13: Energy dependence of the total flux of the photons for the LE, sME ans sHE beams.

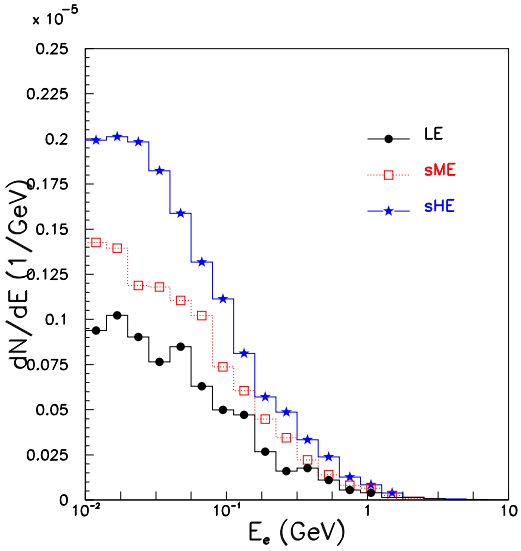

Figure 14: Energy dependence of the total flux of the electrons and positrons for the LE, sME ans sHE beams.

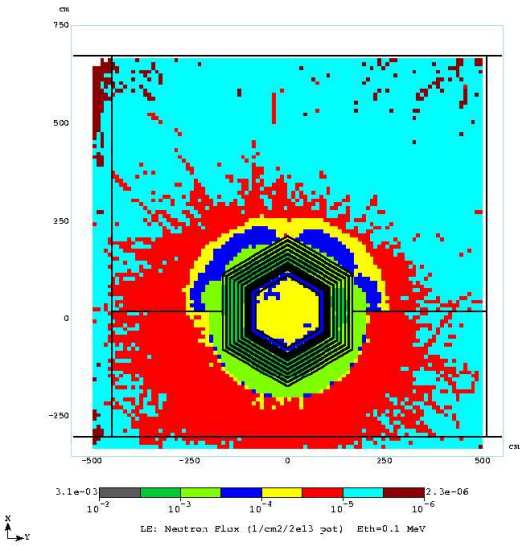

Figure 15: Neutron flux at a NuMI near hall cross-section for the LE beam and E_{th}=0.1 MeV.

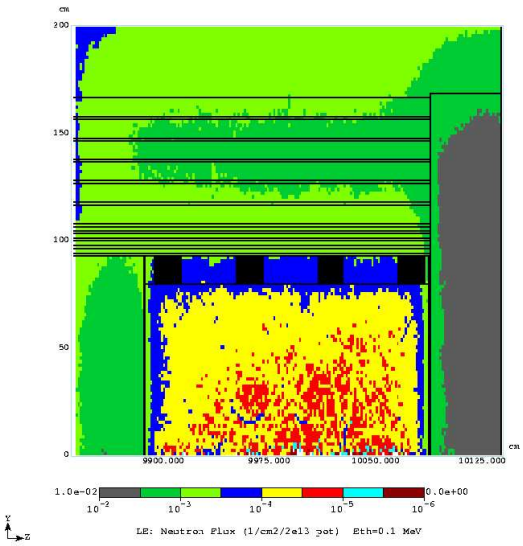

Figure 16: Neutron flux azimuthally averaged about the detector axis for the LE beam and E_{th}=0.1 MeV.

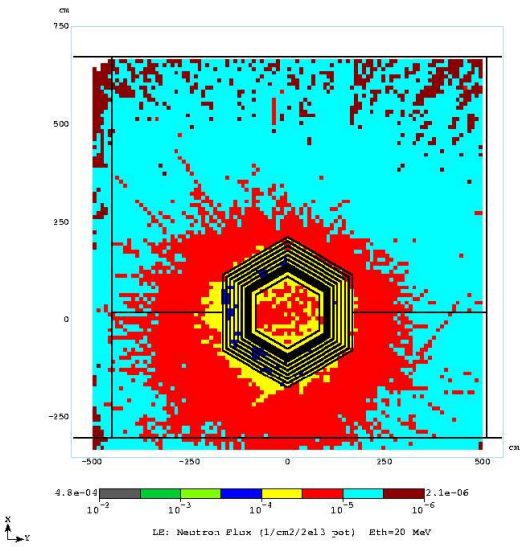

Figure 17: Neutron flux at a NuMI near hall cross-section for the LE beam and E_{th}=20 MeV.

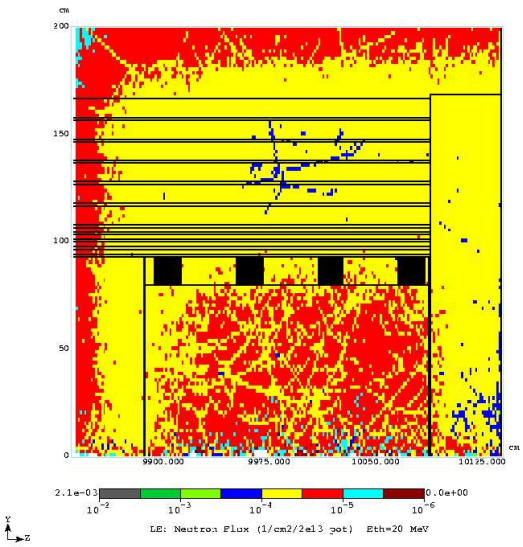

Figure 18: Neutron flux azimuthally averaged about the detector axis for the LE beam and E_{th}=20 MeV.

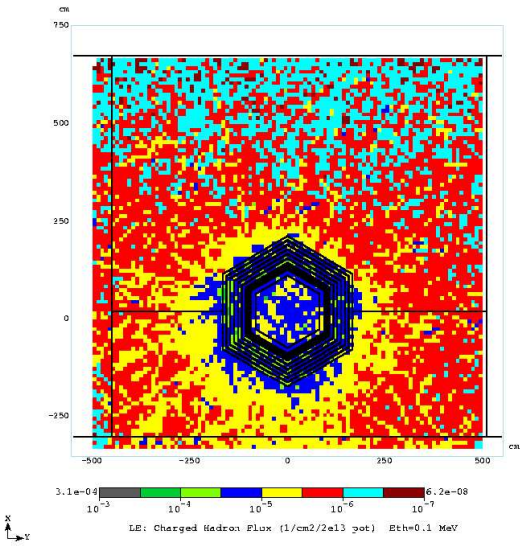

Figure 19: Flux of charged hadrons at a NuMI near hall cross-section for the LE beam and E_{th}=0.1 MeV.

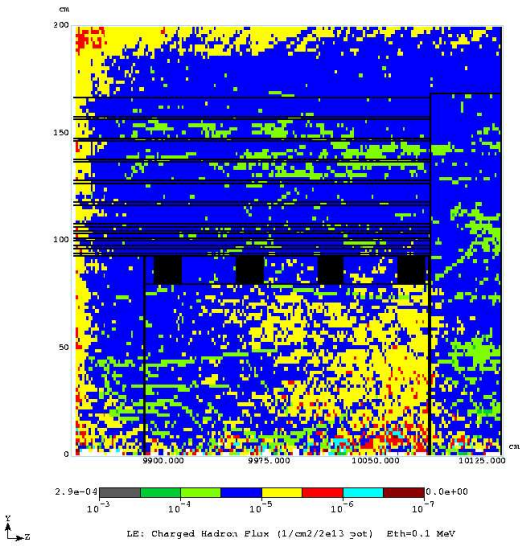

Figure 20: Flux of charged hadrons azimuthally averaged about the detector axis for the LE beam and E_{th}=0.1 MeV.

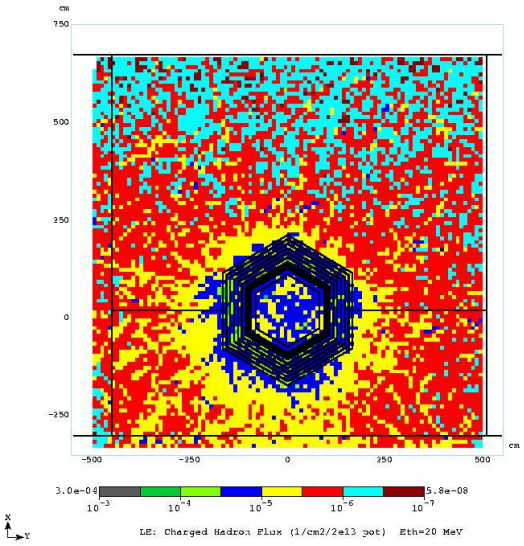

Figure 21: Flux of charged hadrons at a NuMI near hall cross-section for the LE beam and E_{th}=20 MeV.

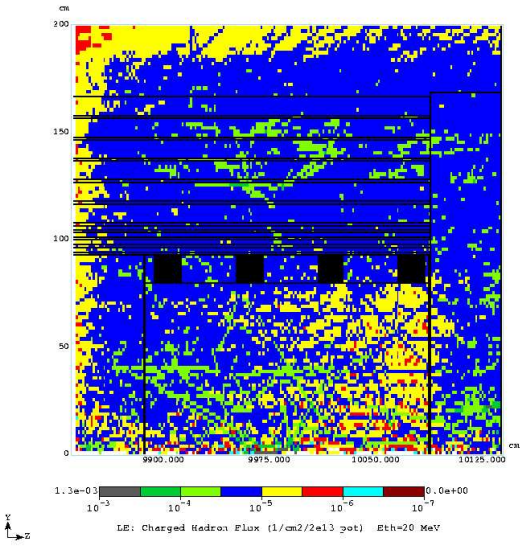

Figure 22: Flux of charged hadrons azimuthally averaged about the detector axis for the LE beam and E_{th}=20 MeV.

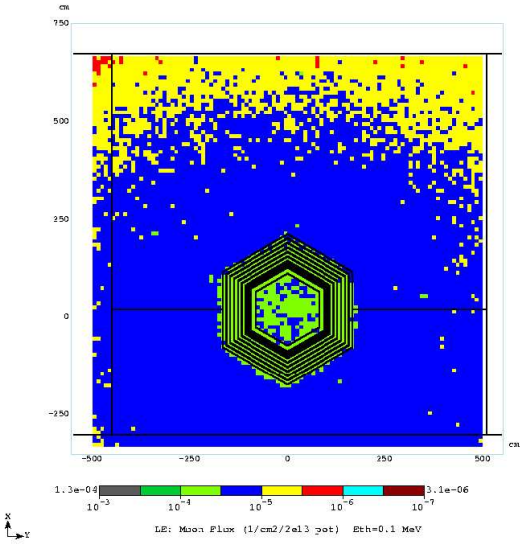

Figure 23: Flux of muons at a NuMI near hall cross-section for the LE beam and E_{th}=0.1 MeV.

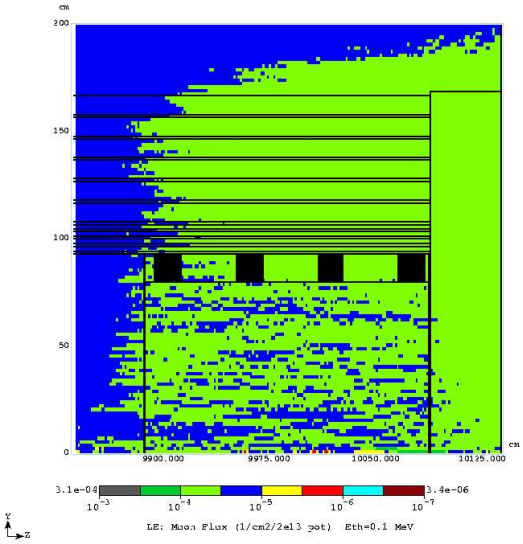

Figure 24: Flux of muons azimuthally averaged about the detector axis for the LE beam and E_{th}=0.1 MeV.

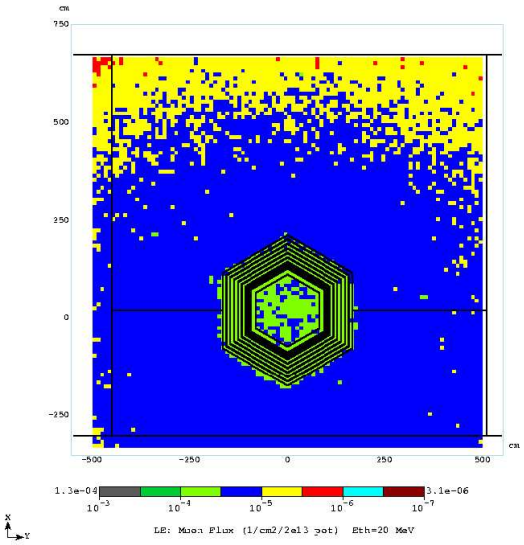

Figure 25: Flux of muons at a NuMI near hall cross-section for the LE beam and E_{th}=20 MeV.

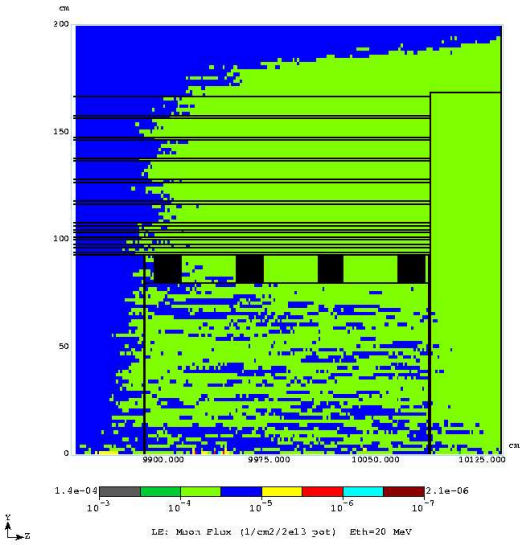

Figure 26: Flux of muons azimuthally averaged about the detector axis for the LE beam and E_{th}=20 MeV.

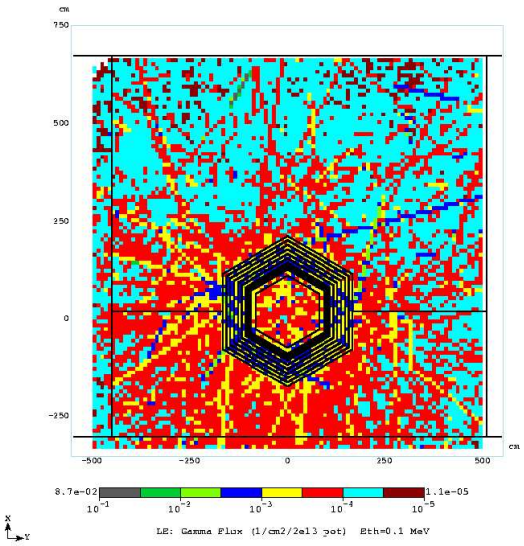

Figure 27: Flux of photons at a NuMI near hall cross-section for the LE beam and E_{th}=0.1 MeV.

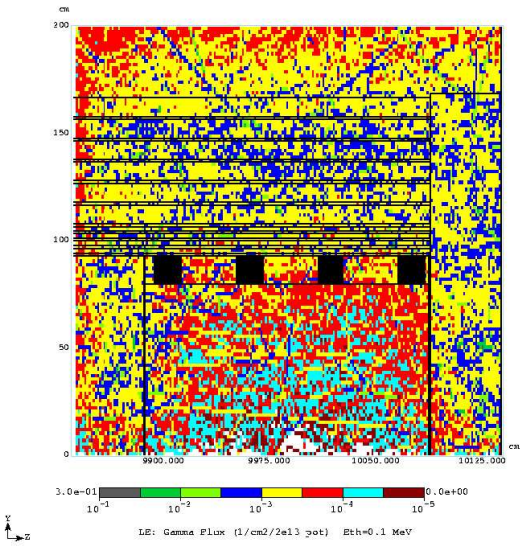

Figure 28: Flux of photons azimuthally averaged about the detector axis for the LE beam and E_{th}=0.1 MeV.

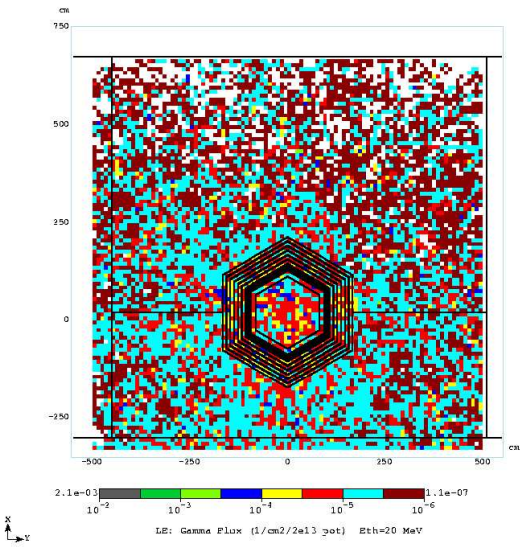

Figure 29: Flux of photons at a NuMI near hall cross-section for the LE beam and E_{th}=20 MeV.

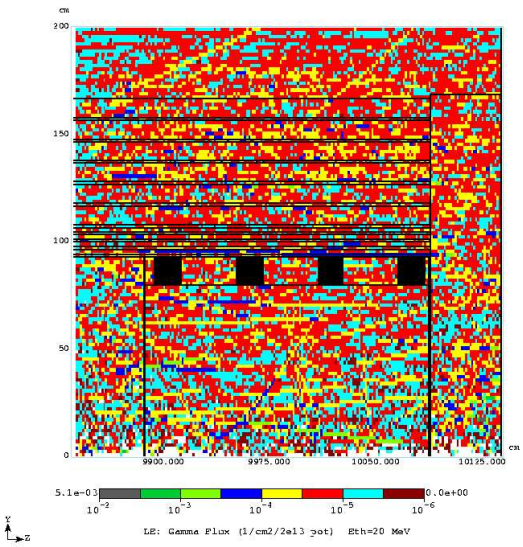

Figure 30: Flux of photons azimuthally averaged about the detector axis for the LE beam and E_{th}=20 MeV.

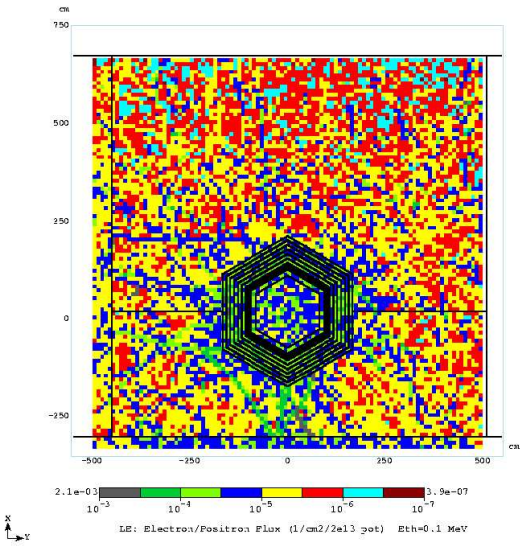

Figure 31: Flux of electrons/positrons at a NuMI near hall cross-section for the LE beam and E_{th}=0.1 MeV.

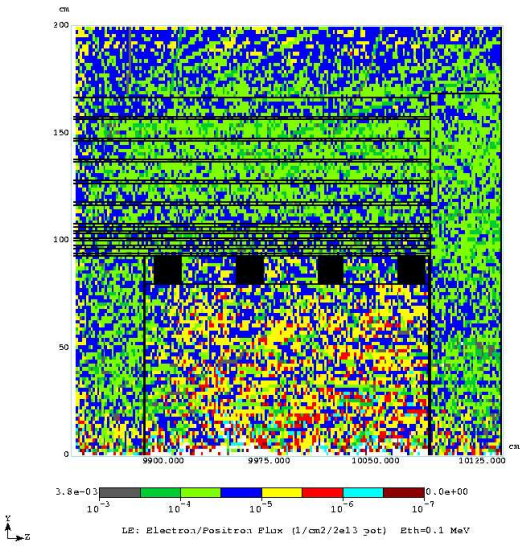

Figure 32: Flux of electrons/positrons azimuthally averaged about the detector axis for the LE beam and E_{th}=0.1 MeV.

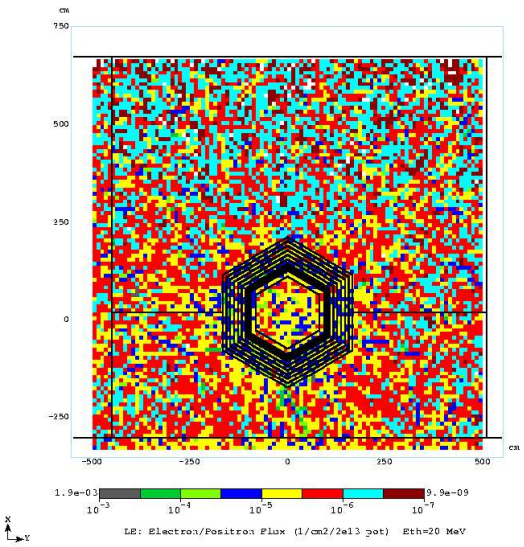

Figure 33: Flux of electrons/positrons at a NuMI near hall cross-section for the LE beam and E_{th}=20 MeV.

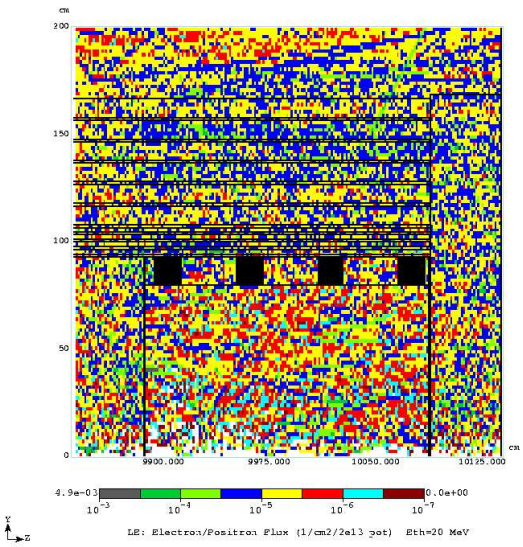

Figure 34: Flux of electrons/positrons azimuthally averaged about the detector axis for the LE beam and E_{th}=20 MeV.